PAPER

Check for updates

One-pot *in situ* synthesis of an NS-ligand co-doped metal–organic framework for the enhanced adsorption-assisted photocatalytic decontamination of metronidazole†

Anwer Hayat, [a] Alamgir, [b] Liangai Huang, [ad] Zongpeng Wang, [ad] Raza Ullah*[c] and Sailing He ⭐ *[ae]

Doping active agents into metal–organic frameworks (MOFs) is widely sought after owing to its potential to enhance adsorption and photocatalytic efficiency, surpassing the potential of bare frameworks. This study incorporated a catalytically active NS-ligand (1,2-benzisothiazolin-3-one) into a very stable and porous PCN-600 MOF *via* an *in situ* synthesis approach. The NS-ligand, which matched with the host ligands of PCN-600, enabled the highly efficient synthesis of NS-co-doped MOFs. The pristine PCN-600 framework and morphology were retained in the MOF altered with the NS-ligand, as demonstrated by XRD, FTIR, and SEM characterizations. A high electron density was generated due to the synergistic effect between the defects in the NS-co-doped photocatalyst and engineered active sites. This facilitated the adsorption-assisted photocatalytic decontamination of metronidazole with an 87% removal by PCN-600-NS-10 compared to 43% by pristine PCN-600 within a total time of 150 min. The MOF doped with the NS-ligand exhibited a reduced band gap and enhanced adsorption and photocatalytic capabilities compared to pristine PCN-600. The impact of operational parameters, such as catalyst dosage, initial solution pH, and MNZ concentration, was also explored. Pseudo-second and pseudo-first order models were found to describe the adsorption and degradation kinetics of metronidazole and the Dubinin–Radushkevich model was found to fit the equilibrium adsorption results. The thermodynamic characteristics of adsorption processes (ΔG_{ads}, ΔH_{ads}, and ΔS_{ads}) demonstrated that adsorption was physical, spontaneous, and exothermic and resulted in increased entropy.

[a]*National Engineering Research Center for Optical Instruments, College of Optical Science and Engineering, Zhejiang University, Hangzhou 310058, People's Republic of China. E-mail: sailing@kth.se*

[b]*School of Materials Science and Engineering, Zhejiang Sci-Tech University, Hangzhou 310018, China*

[c]*College of Materials Science and Engineering, Qingdao University, Qingdao 266071, China. E-mail: razaktk92@gmail.com*

[d]*Taizhou Agility Smart Technologies Co., Ltd, Taizhou, Zhejiang, China*

[e]*Department of Electromagnetic Engineering, School of Electrical Engineering, KTH Royal Institute of Technology, Stockholm, SE-100 44, Sweden*

† Electronic supplementary information (ESI) available. See DOI: https://doi.org/10.1039/d4ra00812j

1. Introduction

Recently, the global environment has been confronted with significant water pollution resulting from pollutants generated by human activities, including industrial, agricultural, and domestic pollution sources.[1,2] In particular, the use of antibiotics can give rise to environmental hazards, including their potential for biological toxicity and the emergence of resistant genes in pathogenic bacteria. These factors pose a significant threat to both the ecological environment and the overall well-being of human society.[3] Metronidazole (MNZ) is classified as a nitroimidazole antibiotic and is commonly employed for the treatment of infections resulting from susceptible parasites and anaerobic bacteria, such as *Trichomonas*, *Giardia*, Vincent's organisms, anaerobic bacteria, and *Entameoba*.[4–6] MNZ is a potentially mutagenic in humans and can cause DNA damage and carcinogenicity.[7] Typically, several antibiotics and other organic contaminants found in water are resistant to decomposition and cannot be completely eliminated using various procedures such as adsorption or ozonation.[6] As a result, it is critical to maintain a healthy environment by removing drugs, preferably, using inexpensive and cost-effective ways.[8]

Conventional methods for treating wastewater containing antibiotics mostly consist of physical, biological, and chemical treatment processes.[9] However, these approaches often encounter challenges, such as partial degradation, significant reliance on the type of antibiotic and water quality, and limited efficiency in degradation. Heterogeneous photocatalytic degradation has become an economical and a promising advanced oxidation technique/process (AOT/AOP) for the treatment of

wastewater. Heterogeneous photocatalysis induces electron and hole pairs in the conduction band (CB) and valence band (VB) of a semiconductor when irradiated with photons that match or exceed the energy gap (E_g) of the semiconductor, typically in the UV and visible regions of light.[10] Electron and hole pair (e^-/h^+) couples can contribute to pollutant degradation directly or indirectly. Photoinduced electrons are powerful reducing agents that may degrade pollutants *via* reduction processes. Semiconductor metal oxides and sulfides, such as titanium dioxide (TiO_2), zinc oxide (ZnO), and zinc sulfide (ZnS), are highly favourable heterogeneous photocatalysts because they are readily available, have a large band gap, and are non-toxic and exceptionally stable.[11,12] Nevertheless, the widespread use of these materials has been constrained by challenges associated with the retrieval of minute particles, their limited adsorption capacity, and as they generally have a large energy gap and a rapid recombination of electrons and holes.[13,14]

Integrated photocatalytic adsorbents (IPCAs) have shown significant promise as a viable alternative to conventional materials for wastewater treatment due to their distinctive characteristics, notably, their capacity to perform multiple roles as both adsorbents and photocatalysts.[15] Metal–organic frameworks (MOFs) are crystalline materials that consist of metal ions and organic ligands. MOFs possess notable attributes, such as a substantial specific surface area, ample porosity, high capacity for drug loading, adjustable pore size, favourable biocompatibility, and customisable surfaces. MOFs have gained significant attention in recent years due to their wide range of applications in adsorption and photocatalysis.[16–19] Hence, creating appropriate MOFs as groundbreaking photocatalytic adsorbents for the effective elimination of waterborne contaminants is desired, but remains a significant obstacle. Decades of research and development have yielded a variety of strategies for the synthesis and modification of catalysts, including atom doping, interface design, and facet control.[20–22] One of the factors that have been demonstrated to significantly impact the coordination structure in MOF materials and consequently alter their catalytic performance is the introduction of non-metallic atoms, particularly heteroatoms, such as nitrogen (N) and sulphur (S), to produce defects in the electronic structure.[20,23] These disruptions occur due to the absence or displacement of atoms or ions.[24] For instance, previous studies have documented that the production of structural defects within MOFs has a discernible impact on both the adsorption and catalytic capabilities.[25,26] The introduction of ligands into the structure of MOFs through doping is an innovative method for inducing the formation of defective MOFs.[20,27] However, researchers continue to face challenges in comprehending and managing the occurrence of defects through the process of ligand doping.[28]

In this study, a ligand containing nitrogen and sulphur atoms (1,2-benzisothiazolin-3-one (BIT)) was incorporated into PCN-600 by a simple and efficient one-pot *in situ* synthesis method. The purpose was to substitute the original linkers present in the structure. The quantity of BIT can govern the occurrence of structural imperfections. The modified structures

exhibited an enhanced migration and separation of photogenerated carriers due to a synergistic effect between newly formed Fe–N active sites and appropriate defects arising from uncoordinated S. Consequently, the electron density was significantly increased at the Fe catalytic sites. The X-ray diffraction (XRD), X-ray photoelectron spectroscopy (XPS), elemental dispersive X-ray spectroscopy (EDS), and FTIR data collectively demonstrated that the incorporation of nitrogen (N) and sulphur (S) into PCN-600 occurred without inducing alterations in its structure and morphology. The incorporation of the NS-ligand into PCN-600 caused a reduced band gap, and facilitated the concurrent integration of adsorption and photocatalytic degradation mechanisms, allowing it to achieve a highly effective elimination of metronidazole from aqueous solutions. We also examined the pH fluctuations, starting concentrations of metronidazole, and catalyst dosage. The thermodynamic properties, specifically the ΔG_{ads}, ΔH_{ads}, and ΔS_{ads}, associated with the adsorption of MNZ onto the NS-ligand doped PCN-600, were assessed. An analysis of the adsorption and degradation kinetics was also conducted.

2. Results and discussions

2.1. XRD and FTIR spectra

The diffraction peak positions of the PCN-600 crystal, particularly those associated with the (100) and (210) planes, closely matched the positions of the generated peaks illustrated in Fig. 1(a). The presence of distinct and persistent diffraction peaks serves as evidence that the PCN-600 sample achieved a high level of crystallization. After NS-ligand doping, the PXRD pattern of the material showed the main characteristic peaks of MOF, verifying the stability of PCN-600. The presence of the principal PXRD peak of PCN-600 indicated that doping with the NS-ligand did not result in framework collapse or phase transition, and could preserve the integrity of the framework. However, the disappearance of some peaks after NS-doping may indicate there were some changes in the inner ordered structures of PCN-600, albeit these had no significant negative effects on the adsorption and degradation performance because of the generation of more active sites that could be used for interactions with light. However, the diffraction peaks in NS-doped MOFs were shifted towards the right compared to those observed in the as-synthesized MOF because of the change in the crystal lattice properties. The primary reason for this shift was the alteration in the volume of the lattice unit cell caused by the disparity in ionic radii between the host lattice ion and the dopant ion. Increasing the size of the dopant ion will lead to an expansion of the unit cell volume while decreasing the size will cause a contraction of the unit cell volume. If the unit cell contracts, this will be seen in the XRD data as a rise in the Bragg angle or a displacement towards the right in the XRD graph. The XRD pattern after activity is shown in S1(a) of ESI Section.†

The functional groups PCN-600, PCN-600-NS-10, and PCN-600-NS-20 were confirmed by Fourier transform infrared (FTIR) spectroscopy, as shown in Fig. 1(b). The peaks observed at around 1650, 1540, and 1500 cm^{-1} represented the stretching vibrations of the carboxyl functional group. The sharp peak at
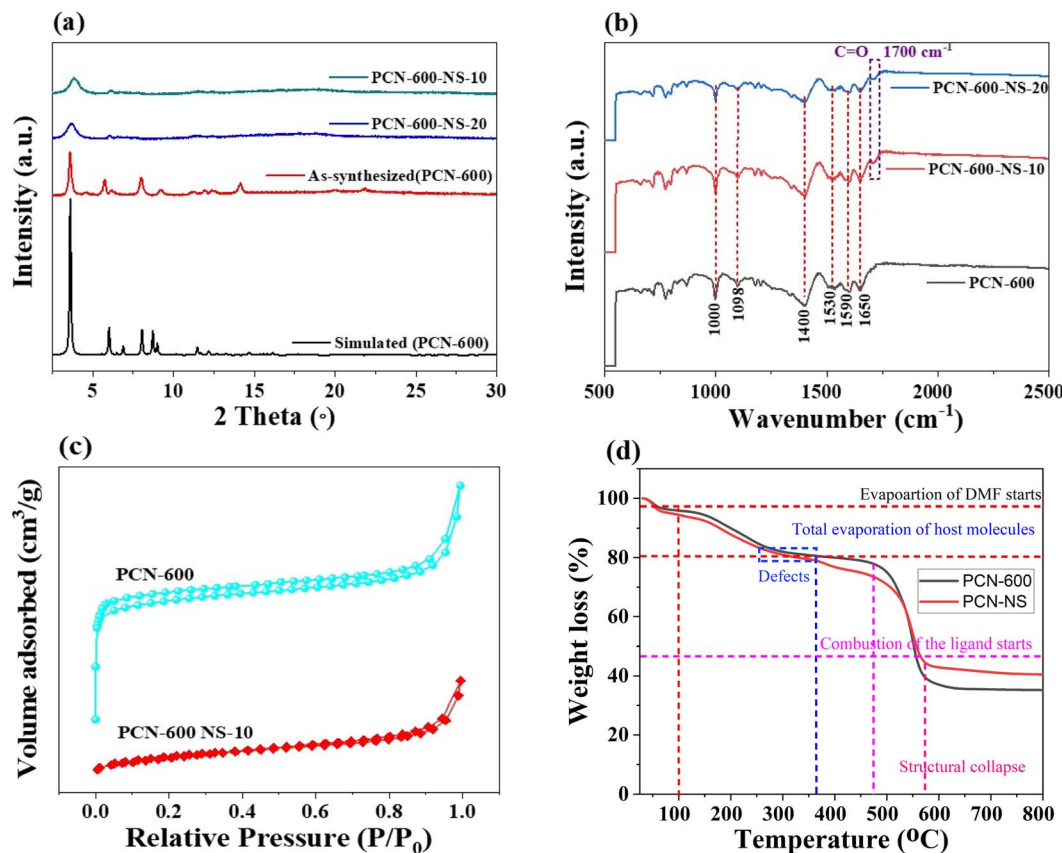
Fig. 1 XRD patterns (a) and FTIR spectra (b) of PCN-600, PCN-600-NS-10, and PCN-600-NS-20, (c) N_2-adsorption–desorption isotherms (c) and thermogravimetric analysis (d) of PCN-600 and PCN-600-NS-10.

about 1400 cm^{-1} was due to the C–O stretching vibration of the carboxylate groups. The peak at about 1000 cm^{-1} was due to the N–H vibrations.[29] In addition, the FT-IR spectra of PCN-600-NS-10 and PCN-600-NS-20 exhibited an extra distinct peak in the range of 1700 cm^{-1}, which was not present in the original PCN-600, attributed to the existence of a carbonyl group (C=O) in the NS-ligand.

2.2. N_2 sorption and thermogravimetric analysis

The porosity analysis of PCN-600 was conducted through N_2-adsorption studies at a temperature of 77 K, as illustrated in Fig. 1(c). The observed type-II isotherms for PCN-600(Fe) and PCN-600-NS-10 indicated microporosity. Notably, the surface area of PCN-600 exhibited a decreasing trend following doping with the NS-ligand. Specifically, the Brunauer–Emmett–Teller (BET) surface area values were found to be 79.80 m^2 g^{-1} for PCN-600 and 25.85 m^2 g^{-1} for PCN-600-NS-10, respectively. Despite the reduction in surface area, the alteration did not have a significant impact on the adsorptive and catalytic activities of the catalysts. This suggests that the functionalization with the NS-ligand did not compromise the catalyst's performance. Examining the N_2-adsorption/desorption isotherms in Fig. 1(e), a type-II isotherm is evident, indicating that the MOF possessed a slit-like mesoporous structure. Additionally, the pore-size distribution was analyzed using the Barret–Joyner–

Halenda (BJH) method, as depicted in Fig. S1(b).† The results demonstrated a mesoporous architecture that became larger after doping with the NS-ligand. This mesoporous structure is noteworthy as it has the potential to enhance mass transfer during catalytic reactions. Further, the increased pore size could facilitate improved accessibility for reactants and products, thereby contributing to the overall efficiency of the catalytic processes involving the MOF catalyst.

Thermogravimetric analysis (TGA) is a commonly used method to measure defects in MOF materials.[30] The weight losses seen over the entire range of the temperature analysis can be attributed to the following processes: first, the weight loss at temperatures below 150 °C was related to the loss of the solvent. Next from 150 °C to 375 °C, there was a mass reduction related to loss of the incomplete ligands. Finally, peaks were observed between 375 °C, and a temperature of 575 °C, which was a sufficient temperature for the full pyrolysis of the substance structure. Typically, the second stage can be ascribed to the degree of defects, as substantiated by a large amount of evidence. In addition, the peak with the greatest elevation in TGA shows relationship between the temperature and weight loss with the most significant reduction occurring between 150 °C and 375 °C. The presence of the maximum defects suggested in the PCN-600-NS-10 framework can be seen in Fig. 1(d).

2.3. Scanning electron microscopy analysis

Fig. 2 displays the surface microstructures of PCN-600 and PCN-600-NS-10, as observed using scanning electron microscopy (SEM). PCN-600 and PCN-600-NS-10 crystals had needle-shaped structures, measuring several μm in length and 500–800 nm in width. The SEM images of the samples obtained after adding the ligand BIT exhibited a needle-shaped morphology, which was consistent with that of pristine MOF but with a much rougher surface, even with some slight buds. The EDX (Fig. 2(c)) and elemental mapping distribution of PCN-600 (Fig. 2(b)) demonstrated a homogeneous distribution of Fe, C, N, and O along the long axis of the PCN-600 single crystal microwares, suggesting that PCN-600 consisted of these elements and exhibited excellent crystallization. The EDX (Fig. 2(f)) and mapping distribution of PCN-600-NS-10 (Fig. 2(e)) showed that, along with Fe, C, N, and O, the elements of the doped ligand, *i.e.*, S and N, were also present and evenly distributed. The SEM image after activity is depicted in S1(c) of the ESI.†

2.4. X-ray photoelectron spectroscopy (XPS)

X-ray photoelectron spectroscopy (XPS) was employed for the analysis and determination of the surface chemical elements and the chemical state of the catalysts. Fig. 3(a–e) present the high-resolution spectra for PCN-600-NS-10, including for the C 1s orbital (Fig. 3(a)), revealing two distinct surface components associated with carbon elements within the ligand structure. These components were manifested at binding energies of 287.3 eV, corresponding to the C=O bond, and 284.2 eV, attributed to the C=C in the TCCP linker of PCN-600.

In the O 1s spectrum, a notable peak appeared at approximately 529.5 eV, which was assigned to the Fe–O, while the peaks at 531 and 532 eV were indicative of oxygen vacancies, signifying the presence of surface hydroxyl groups.

XPS analysis of the Fe 2p spectrum revealed two distinct binding energy peaks. The first peak, observed at around 711.1 eV, was associated with the Fe 2p$_{3/2}$ orbital, while the second peak at approximately 724.4 eV corresponded to the Fe 2p$_{1/2}$ orbital. The N 1s and Fe 3d peaks were derived from the grafted PCN-600, with a single signal detected at approximately 398 eV for the N 1s electron binding energy. Additionally, peaks were observed at 710.3 and 724.1 eV, attributed to the Fe 2p 3/2 and 1/2 electron binding energies, respectively, providing evidence of the effective attachment of the Fe-TCPP compound to the NS-ligand.

Upon closer examination of the N 1s spectrum, two distinct signals could be seen to emerge at 400.4 and 398 eV, attributed to the chemical species Fe–N and carbonitrile, respectively. Similarly, the corresponding peak at 165 eV indicated the presence of S–C in the synthesized structure. These findings collectively offer clear evidence of the successful fabrication of the NS@PCN-600 structure.

2.5. Band gap analysis

Solid-state UV-vis spectroscopy is a valuable technique for investigating the electronic transitions, optical properties, and photosensitivity of powdered solid samples.[31,32] Therefore, UV-vis spectroscopy analysis of PCN-600 and PCN-600-N,S-10 was performed in the solid state to investigate their changes in optical properties. The typical UV-visible absorption spectra of PCN-600 and PCN-600-N,S-10 exhibited distinct peaks in the visible region, as shown in Fig. S2 of the ESI Section.† The Tauc plot was employed to compute both the allowed direct and allowed indirect band gaps. The formula used for this
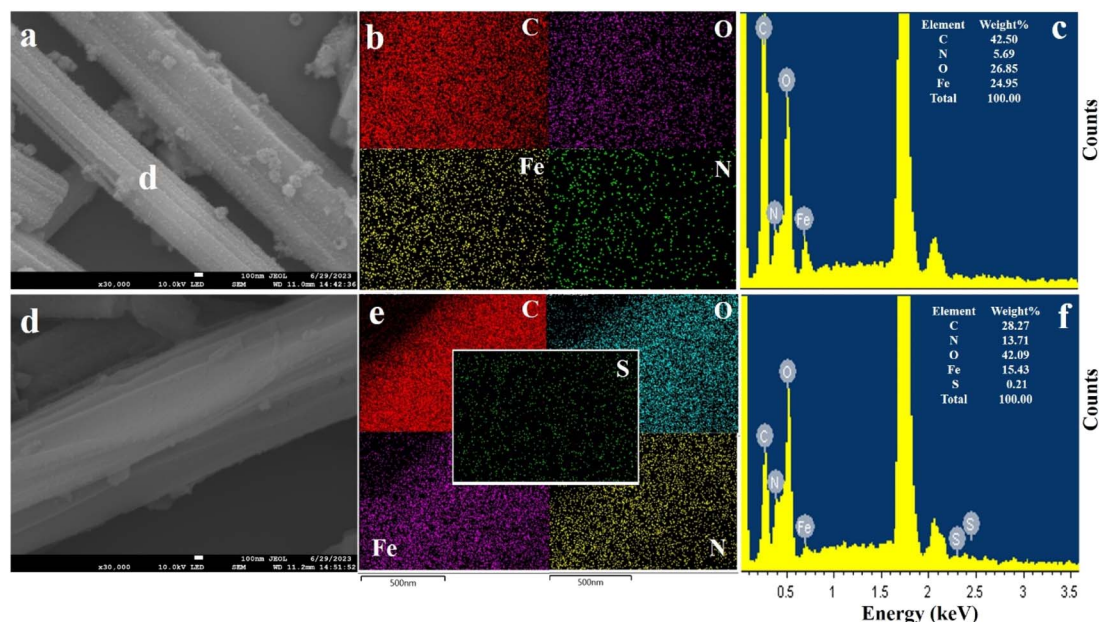

Fig. 2 SEM image of PCN-600 (a), elemental mapping distribution of PCN-600, (b) EDX spectra of PCN-600 (c), SEM image of PCN-600-NS-10 (d), elemental mapping distribution of PCN-600-NS-10 (e), and EDX of PCN-600-NS-10 (f).
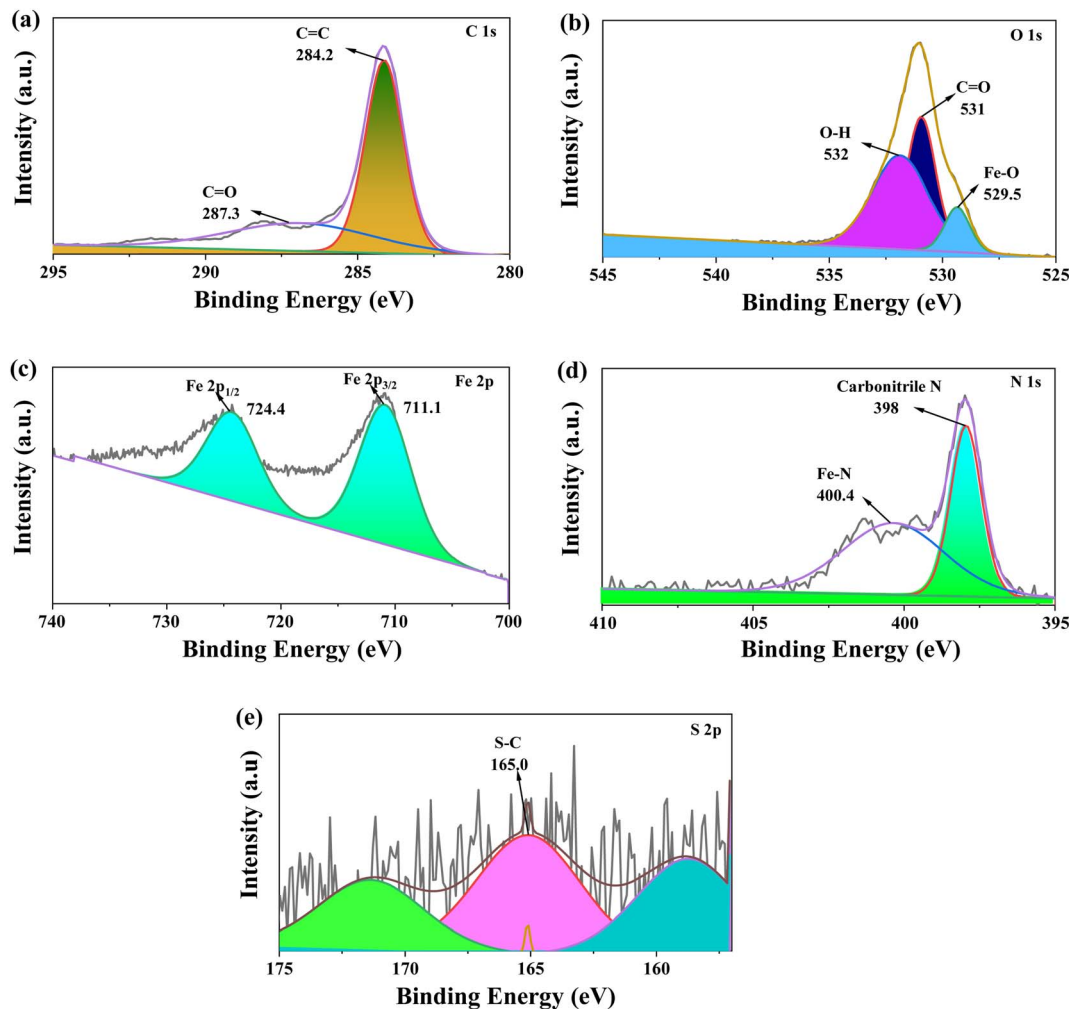
Fig. 3 XPS spectra of PCN-600-NS-10; (a) C 1s, (b) O 1s, (c) Fe 2p, (d) N 1s, and (e) S 2p.

calculation is $(Ah\upsilon)^n = C(h\upsilon - E_g)$, where A represents the absorbance, h denotes Planck's constant, υ represents the frequency, and E_g represents the energy of the band gap. The index n has a value of 2 and $\frac{1}{2}$ for the allowed direct and indirect band gap values of the catalyst. The plot of $(Ah\upsilon)^n$ as a function of $h\upsilon$ was drawn, and by extrapolating the linear section of the plot to the y-axis where it intersects at y-axis $= 0$, different values for the band gap energy were obtained for $n = 2$ and $\frac{1}{2}$. The allowed indirect band gap and allowed direct band gap of PCN-600 were thus determined to be 2.89 and 2.50 eV, respectively, as observed in Fig. S2,† indicating its capability to absorb visible light. However, the introduction of N and S dopants in PCN-600 resulted in a decrease in its band gap. As a result, PCN-600-NS-10 demonstrated relatively small band gaps of 2.53 and 2.18 eV (Fig. S2†) for direct and indirect transitions, respectively.

2.6. Adsorption and photocatalytic performances

The performance of the synthesized samples in terms of adsorption and photocatalytic degradation was assessed by conducting experiments on the adsorption-assisted photocatalytic degradation of MNZ in an aqueous solution.

Adsorption plays a crucial role in the context of heterogeneous photocatalysis to eliminate antibiotics from wastewater. MOFs as integrated photocatalytic adsorbents (IPCAs) have demonstrated synergistic characteristics, resulting in enhanced removal efficiencies through a combination of photocatalytic degradation and adsorption processes. The process of adsorption facilitates the concentration of pollutant molecules on the surface of the IPCA, hence enhancing their availability to reactive sites and subsequently leading to an improvement in the rate of degradation. The adsorptive and photocatalytic capabilities of PCN-600 doped with NS-ligands were evaluated and compared to those of the unmodified PCN-600 material.

Before the exposure to visible light, a dark adsorption experiment was conducted to examine the equilibrium of adsorption and desorption. Fig. 4(a) illustrates the impact of the adsorption and photocatalytic degradation on the elimination of MNZ when employing various types of IPCAs. Adsorption was found to proceed rapidly, followed by a comparatively slower rate of photocatalytic degradation. As revealed in Fig. 4(a), the pristine PCN-600 adsorbed about only 12% of MNZ with an adsorption capacity of 24 mg g^{-1} at adsorption equilibrium. The
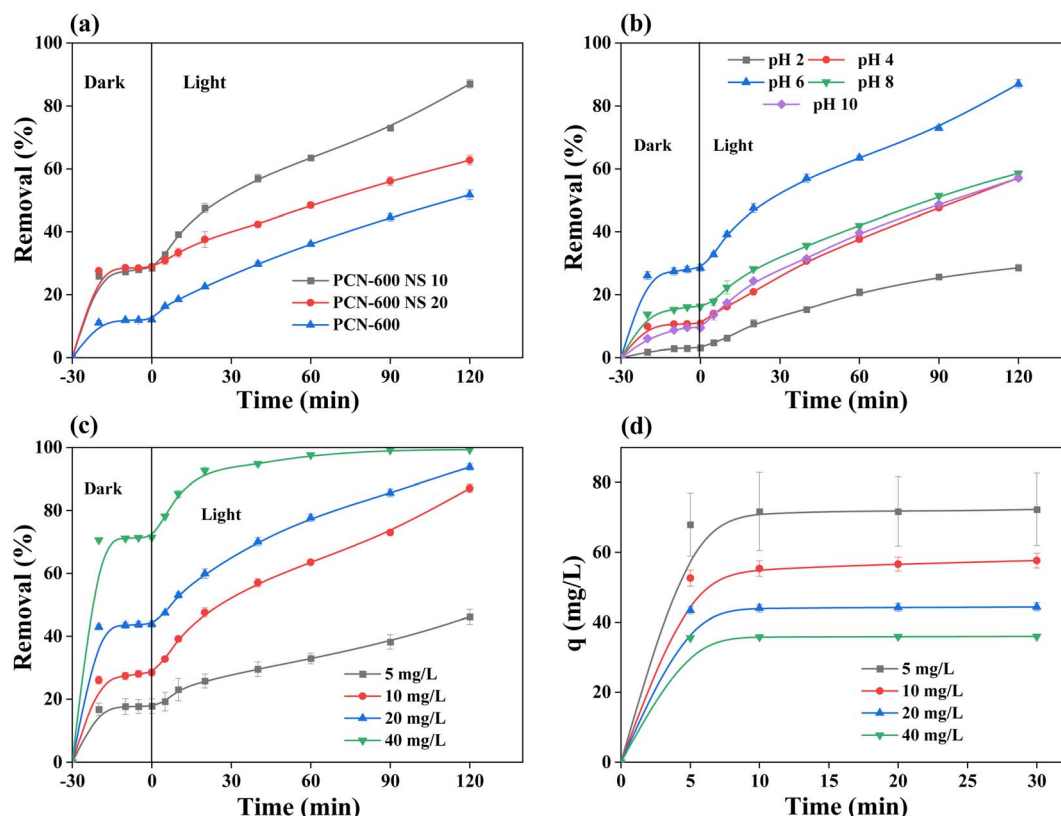
Fig. 4   Effect of the type of catalyst on the removal of metronidazole. Conditions: catalyst dose = 0.01 g L^{-1}, MNZ conc. = 20 mg L^{-1}, pH = 6, room temperature (RT) (a). Effect of the initial pH of the solution on the removal of metronidazole using PCN-600-NS-10; conditions: catalyst dose = 0.01 g L^{-1}, MNZ conc. = 20 mg L^{-1}, RT (b). Effect of the dose of PCN-600-NS-10; conditions: MNZ conc. = 20 mg L^{-1}, pH = 6, RT, (c). Adsorption capacity of 10%-NS PCN-600 using different initial doses (d).

adsorption equilibrium performances of PCN-600-NS-10 and PCN-600-NS-20 reached about 28% and 29% adsorption of MNZ, with corresponding adsorption capacities of 57 and 58 mg g^{-1}, respectively. After 30 min, the adsorption did not exhibit any notable change, as the repulsive interactions between the adsorbed MNZ molecules and the molecules in the solution were enhanced.[33] Furthermore, the pseudo-second rate constants of MNZ adsorption onto PCN-600, PCN-600-NS-10, and PCN-600-NS-20 were found to be 0.053, 0.124, and 0.12 g mg^{-1} min^{-1}, respectively, as shown in Fig. S6(a) of the ESI Section.†

To assess the photocatalytic performance of various integrated photocatalytic adsorbents, photodegradation tests of MNZ were conducted under illuminated conditions following in-the-dark adsorption. As shown in Fig. 4(a), when PCN-600 was exposed to visible light, it was able to remove approximately 40% of MNZ after adsorbing 12% of it. In total, the removal efficiency reached 52%. PCN-600-NS-10 and PCN-600-NS-20 exhibited significantly greater activity than the original PCN-600 when exposed to visible light. The removal efficiency of the NS-ligand-doped PCN-600 IPCAs was reduced as the NS-ligand content was increased. The catalyst PCN-600-NS-10 exhibited the greatest efficacy, as depicted in Fig. 4(a), achieving an 87% decline in MNZ concentration. This reduction was achieved through a combination of 28% adsorption and

59% photocatalytic degradation within a total reaction time of 150 min. Moreover, the pseudo-first order rate constants of degradation of MNZ were in the order of 0.0045, 0.0129, and 0.0054 min^{-1} for PCN-600, PCN-600-NS-10, and PCN-600-NS-20, respectively (Fig. S7(a)†). Hence, the catalyst PCN-600-NS-10 was chosen as the most suitable catalyst for subsequent investigations.

2.7. Effect of the pH

The surface charge of the photocatalyst and the ionization of the adsorbate are significantly influenced by the pH of the reaction medium, which in turn has a substantial impact on the removal of organic pollutants in wastewater.[34] As depicted in Fig. 4(b), the removal of MNZ exhibited an initial increase as the pH level rose, achieving maximum efficacy at pH 6, and a removal rate of 87%. Subsequently, the removal efficiency diminished as the pH level continued to rise beyond 6. The reason for this phenomenon could be attributed to the positively charged nature of the catalyst surface at pH values lower than the point of zero charge (pH$_{pzc}$). This positive charge impedes the adsorption of cationic MNZ, resulting in a low rate of removal, as illustrated in Fig. 4(b). The catalyst surface exhibits a negative charge when the pH is greater than the point of zero charge (pH$_{pzc}$) due to the presence of abundant hydroxyl groups on its surface. This characteristic facilitates the

adsorption of MNZ, hence increasing the rate of removal. At low pH levels, notably pH 2 and 4, there was competition between MNZ and H$^+$ ions for adsorption. This competition led to a decrease in the quantity of MNZ that could reach the negatively charged surface of the catalyst. Consequently, the removal efficiency was reduced. Additionally, the anions of the acid, *i.e.*, Cl$^-$ ions, were able to react with hydroxyl radicals, leading to inorganic radical ions (ClO$^-$ radicals). These inorganic radical anions displayed a much lower reactivity than the radical ˙OH,[35] so that they do not take part in MNZ removal. At pH greater than six, the adsorption capacity and removal rate diminished. This occurred due to the emergence of repulsive interactions between the catalyst surface, which was strongly negatively charged, and the loosely bound electron pairs of the MNZ. Therefore, the electrostatic force of repulsion between these charges caused the MNZ molecules to be pushed away from the surface of the catalyst. Despite the potential for the increased formation of ˙OH radicals and improved degradation extent at higher pH levels, the repulsive force described above outweighed these beneficial effects.[36] Moreover, radical–radical reactions occur at higher pH levels as a result of the large amount of ˙OH radicals present,[35] thereby further declining the removal rate of MNZ.

In addition, it is worth noting that metronidazole exhibits a pK_a value of 2.55. Consequently, in acidic conditions, metronidazole carries a positive charge. This positive charge leads to repulsive interactions between MNZ and PCN-600-NS-10, resulting in a decline in the removal efficacy of MNZ. At a pH close to neutrality, there is no repulsive interaction between PCN-600-NS-10 and the MNZ. Therefore, the adsorption of pollutants tends to increase within the adsorbent, thereby improving the removal efficiency at a pH of 6. Attaining an optimal pH within the neutral range is highly desirable for the removal process due to its efficiency and cost-effectiveness, making it a viable option for large-scale implementation. A comprehensive examination of many studies additionally revealed that the optimal pH for the adsorption process of MNZ falls within the neutral range.[37,38]

2.8. Effect of the catalyst dose

The adsorption and degradation properties can be considerably influenced by the dosage of the integrated photocatalytic adsorbent.[39] The investigation here was focused on the dosage of the adsorbent within the range of 5–40 mg L^{-1}. The outcomes of this investigation are visually represented in Fig. 4(c). As depicted in Fig. 4(c), there was a positive correlation between the dosage of the adsorbent and the removal percentage of MNZ. This indicated a direct relationship between the amount of adsorbent used and the rate of adsorbate removal. It can be seen that 46%, 87%, 94%, and 99% removal of MNZ was achieved using 5, 10, 20, and 40 mg L^{-1}, respectively, of PCN-600-NS-10 as an IPCA. It can be observed from Fig. 4(d) that the adsorption capacity of MNZ was reduced with the increase in the dosage of the adsorbent. The adsorption capacity of MNZ exhibited a gradual decline, ranging from 72 to 36 mg g^{-1} when the dosage of the adsorbent was increased from 5 to 40 mg L^{-1}.

The highest adsorption capacity of MNZ on PCN-600-NS-10 was achieved when the adsorbent dosage was 5 mg. However, the overall removal efficiency remained relatively low. After considering the adsorption capacity and elimination percentage, a dosage of 10 mg was ultimately chosen as the best dose for the subsequent investigations.

2.9. Effect of the initial concentration of MNZ

In practical wastewater treatment, the initial concentration of pollutants is a critical determinant in attaining a satisfactory level of removal efficiency. Fig. 5 displays the findings of a study examining the impact of the initial MNZ concentrations, which varied between 10 and 30 mg L^{-1}. The influence of the initial MNZ concentration on the adsorption process was obvious as 44%, 29%, and 25% of MNZ was eliminated at initial MNZ concentrations of 10, 20, and 30 mg L^{-1}, respectively. After 30 min of adsorption, PCN-600-NS-10 could effectively eliminate MNZ despite its relatively low initial concentration. This has substantial implications for industrial applications. The observation that the removal efficiency declined as the initial MNZ concentration increased was consistent with previous research.[40] However, the adsorption capacity was increased from 46.9 to 74.4 mg g^{-1} with increasing the initial MNZ concentration from 10 to 30 mg L^{-1}, as depicted in Table 1. The availability of a small number of molecules and redundant MOF adsorption sites could explain the low adsorption capacity of MNZ at low concentrations. Raising the initial MNZ concentration would enhance the concentration gradient between the surface of MOF and the solution. Then, MNZ molecules may easily overcome the impedance to mass transfer between a solid and a liquid and adhere to the adsorption sites of MOFs.[41]

Further investigation was conducted to assess the degradation performance of MNZ at an increasing initial concentration after the establishment of adsorption–desorption equilibrium. The photocatalytic degradation of MNZ exhibited a decline as the initial concentration rose from 10 to 30 mg L^{-1}. Degradations of 59% and 42% were observed at low concentrations of 10 and 20 mg per L MNZ, respectively, while degradation was reduced to 29% at a higher concentration of 30 mg L^{-1}. This was because, hydroxyl radicals have an incredibly short lifespan, lasting only a few nanoseconds, and as a result, they are only able to undergo reactions in the location where they are generated. Enhancing the MNZ molecule concentration per unit volume logically amplifies the probability of collision between organic matter and oxidizing species, resulting in a surge of the degradation efficacy. It was observed that the degrading efficacy of MNZ was reduced as the starting concentration was increased from 10 to 30 ppm. The decrease in degradation percentage with the increase in MNZ concentration could be attributed to two factors. As the concentration of MNZ increases, a greater number of molecules will adhere to the surface of the photocatalysts, resulting in a decrease in the number of active sites on the catalysts. Consequently, when the catalyst surface area increases, the production of hydroxyl radicals will decrease. In addition, a higher concentration of MNZ can result in a reduction in the number of photons
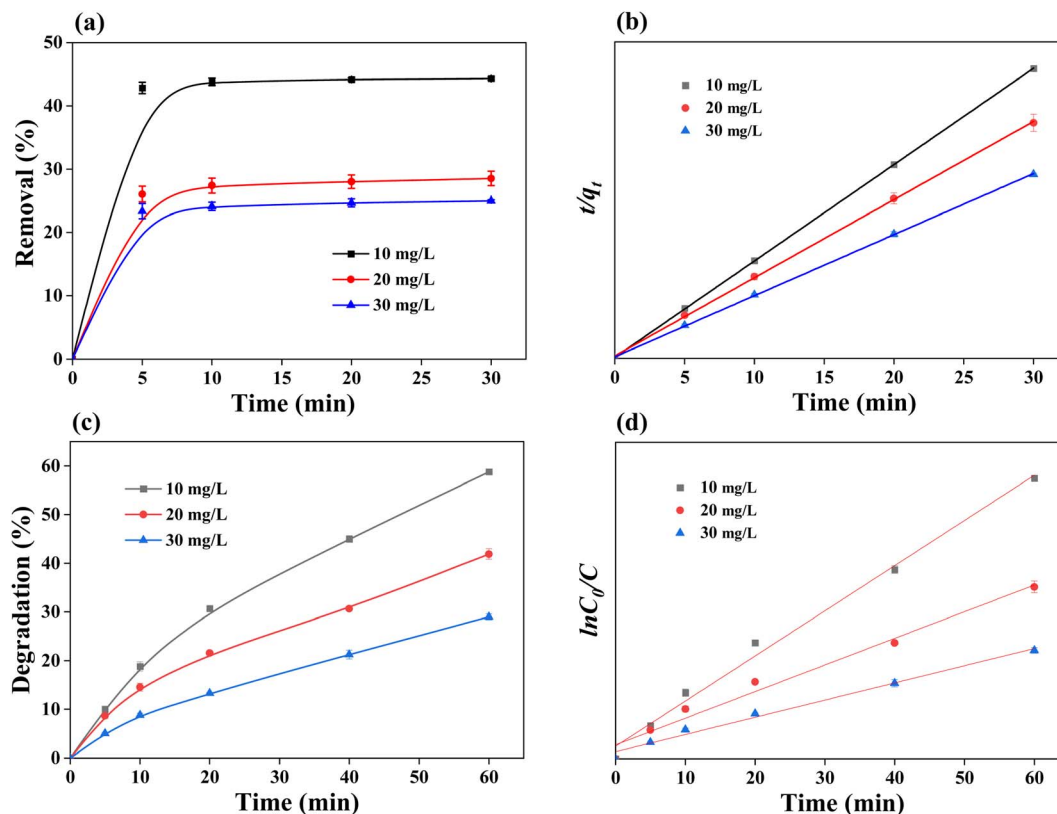
Fig. 5 Effect of the initial concentration of metronidazole on the adsorption performance (a), degradation performance (c), adsorption kinetics (b), and degradation kinetics (d) using 10%-NS PCN-600. Conditions: catalyst dose = 0.01 g L^{-1}, pH = 6, room temperature (RT).

reaching the catalyst's surface. Molecules of MNZ absorb a greater amount of light, resulting in a decrease in the excitation of photocatalyst particles by photons. These results are consistent with the findings reported in the literature.[21,42]

The adsorption rate and degradation mechanism of MNZ utilizing PCN-600-NS-10 were analyzed by examining the pseudo-first order and pseudo-second-order models at three different concentrations using the following equations.

$$\log(q_e - q_t) = \log q_e - \left(\frac{k_1}{2.303}\right)t \tag{1}$$

$$\frac{t}{q_t} = \frac{1}{k_2 q_e^2} + \frac{t}{q_e} \tag{2}$$

where q_e and q_t are the amounts of MNZ adsorbed at equilibrium and at time t, and k_1 and k_2 are pseudo-first and pseudo-

second order rate constants, respectively. The plot of the linear form of the pseudo-second order is shown in Fig. 5(b). Based on the correlation co-efficient (R^2) values, the adsorption kinetic data were accurately characterized by the pseudo-second-order model, as shown in Table 1. As indicated in Table 1, the adsorption rate constant (k_2) decreased with increasing the initial concentration of MNZ. The adsorption kinetics could be described using a pseudo-second-order model, in which the adsorption rate is controlled by chemical adsorption, and the adsorption capacity is determined by the number of active sites on the adsorbent.[43]

The degradation kinetics of MNZ were found to follow the pseudo-first-order model, as depicted in Fig. 5(d). A straight line was obtained by plotting ln C_0/C vs. reaction time, with regression co-efficient (R^2) values >0.97, exhibiting that the pseudo-

Table 1 PSO and PFO kinetic parameters for the adsorption and degradation, respectively, of MNZ using PCN-600-NS-10

| MNZ concentration (mg L^{-1}) | Adsorption | | | | | Degradation | | |
| | | q_e (mg g^{-1}) | | | | | | |
	Removal (%)	q_{eexp}	q_{ecalc}	k_2 (g mg^{-1} min^{-1})	R^2	Removal (%)	k_1 (min^{-1})	R^2
10	44	46.8	46.9	0.273	0.999	59	0.0143	0.992
20	29	57.6	57.8	0.121	0.999	42	0.0084	0.979
30	25	74.1	73.7	0.0575	0.999	29	0.0054	0.988

first-order model was best suited for describing the degradation kinetics. The degradation rate constant values were found to decrease with increasing the initial concentration, indicating there would be less degradation for higher concentration values. The parameters of the kinetic model are presented in Table 1.

2.10. Activation energy of adsorption

To determine the activation energy, the adsorption process was carried out at three different temperatures (298, 318, and 338 K). The determination of the activation energy (E_a) can provide insights into the physical or chemical characteristics of adsorption. In the case of physical adsorption, the energy required for activation is typically minimal (<4.2 kJ mol^{-1}), and the attainment of equilibrium occurs swiftly, and is often reversible. The investigation here involved calculating the activation energy (E_a) of the reaction rate's temperature dependency. This was done by examining the adsorption process at three distinct temperatures (298, 318, and 338 K) using the linear form of the Arrhenius equation,[44,45] as given below.

$$-lk_{app} = -\ln A + \frac{E_a}{RT} \quad (3)$$

A typical Arrhenius plot was made by plotting the natural logarithm of the k-values obtained at different temperatures *versus* the reciprocal of the temperature. The activation energy for the MNZ adsorption process was determined to be around 2.99 kJ mol^{-1} based on the slope of the curve. As depicted in Fig. S3(a and b) of the ESI,† the comparatively low value of E_a, approximately 2.99 kJ mol^{-1} for the adsorption of MNZ, clearly indicated that the adsorption process was physical and proceeded with a negligible energy barrier.

2.11. Thermodynamics of the adsorption of MNZ

Thermodynamic analysis was conducted to determine the spontaneity and thermodynamic nature (endothermic or exothermic) of the adsorption process. The results in Table 2 demonstrate that the adsorption capacity of MNZ increased as the reaction temperature increased. This could be attributed to the enhanced collision frequency between MNZ molecules and the adsorbent surface. The thermodynamic variables (ΔG_{ads}, ΔH_{ads}, and ΔS_{ads}) were determined by examining the adsorption process at three different temperatures (293, 313, and 333 K) through utilization of the following reactions:[46]

$$\Delta G_{ads} = -RT \ln K_d \quad (4)$$

$$\Delta G_{ads} = \Delta H_{ads} - T\Delta S_{ads} \quad (5)$$

where R indicates the universal gas constant, which has a numerical value of 8.314 J mol^{-1} K^{-1}; T denotes the absolute temperature; and K_d signifies the distribution co-efficient, which is defined as the quotient of the quantity of MNZ adsorbed (mg g^{-1}) and the concentration of the MNZ in the solution (mg L^{-1}) at the point of equilibrium.

ΔG_{ads} values ranging from 0 to −20 kJ mol^{-1} suggest modest physical adsorption, while those between −20 and −80 kJ mol^{-1} indicate chemisorption. As listed in Table 2, the negative values for standard ΔG_{ads} suggest that the adsorption of MNZ was a spontaneous and viable process. Furthermore, the range of ΔG_{ads} indicates the physical characteristics of the adsorption. As the temperature increased, the adsorption capacity was enhanced, and the absolute value of ΔG_{ads} increased (Table 2), indicating that the adsorption process became more favourable at higher temperatures.

The enthalpy change (ΔH_{ads}) and entropy change (ΔS_{ads}) values associated with the adsorption process were determined by analyzing the intercept and slope of the ΔG_{ads} against temperature (T) plot, as depicted in Fig. S3(b).† Table 2 displays there was a negative ΔH_{ads} value of around −4.05 kJ mol^{-1}, which signifies the exothermic characteristic of the process. The range of ΔH_{ads} suggests that MNZ was physically adsorbed onto the surface of PCN-200-NS-10. The observed positive change in entropy (ΔS_{ads}) of approximately 25.2 J mol^{-1} K^{-1} indicates a dissociation mechanism and an enhanced level of disorder at the solid–liquid interface during the adsorption process of MNZ.

2.12. Equilibrium isotherms

The adsorption isotherm is a valuable tool for understanding the underlying mechanism of the adsorption process. Hence, the quantity of MNZ adsorbed at the point of equilibrium onto PCN-600-NS-10 was determined at different beginning temperatures, and the findings are depicted in Fig. S4 of the ESI Section.† The experimental data were fitted using three commonly employed adsorption models, namely the Langmuir model, Freundlich model, and Dubinin–Radushkevich model. The calculated parameters are shown in Table 3.

The Langmuir sorption isotherm is commonly employed to explain the process of adsorption from a solution. It is applicable when a monolayer of molecules is adsorbed onto a surface that has a limited number of identical sites. The Langmuir adsorption isotherm was used in its linear version,[47] as expressed below:

Table 2 Thermodynamic parameters for the adsorption of metronidazole onto PCN-600-NS-10

Temperature (K)	k_{app} (g mg^{-1} min^{-1})	q_m (mg g^{-1})	C_e (mg L^{-1})	K_d	ΔG_{ads} (kJ mol^{-1})	ΔH_{ads} (kJ mol^{-1})	ΔS_{ads} (J mol^{-1} K^{-1})
298	0.173	57.8	14.3	4.0	−2.48	−4.05	25.2
318	0.161	62.5	13.9	4.4	−2.64		
338	0.15	66.7	13.6	4.9	−2.81		

RSC Advances

Table 3 Langmuir, Freundlich, and Dubinin–Radushkevich adsorption isotherms parameters at different temperatures

Temperature (K)	Langmuir isotherm			Freundlich isotherm			Dubinin–Radushkevich isotherm			
	q_m (mg g^{-1})	K_L (L mg^{-1})	R^2	K_F (mg g^{-1})	n_F	R^2	β (mol^2 J^{-2})	q_m (mg g^{-1})	E (J mol^{-1})	R^2
293	14.95	−0.093	0.999	72 403	−0.441	0.999	5×10^{-5}	13.82	100.0	0.999
313	18.80	−0.103	0.999	25 336	−0.439	0.999	4×10^{-5}	18.95	111.8	0.999
333	21.14	−0.108	0.999	15 522	−0.478	0.999	3×10^{-5}	22.13	129.1	0.999

$$\frac{C_e}{q_e} = \frac{1}{K_L q_m} + \frac{C_e}{q_m} \tag{6}$$

where C_e is the equilibrium concentration (mg L^{-1}); (q_e) is the equilibrium adsorption capacity, which represents the maximum amount of adsorbate that can be adsorbed per unit volume at equilibrium, also measured in mg L^{-1}; q_m is the maximum monolayer coverage capacity, which refers to the maximum adsorption capacity of the adsorbent material in mg L^{-1}; and K_L is the Langmuir isotherm constant, which is a parameter in the Langmuir adsorption isotherm equation, expressed in units of L mg^{-1}. A plot of C_e/q_e *vs.* C_e should indicate a straight line of slope $1/q_m$ and an intercept of $1/q_m K_L$. The analysis of the experimental data, as presented in Table 3, reveals that the Langmuir approach was employed to examine the adsorption behaviour of MNZ at three distinct temperatures (293, 313, and 333 K). The obtained results indicated negative intercepts, hence indicating a deviation from the Langmuir approach in the adsorption behaviour of MNZ.

The Freundlich isotherm is a more comprehensive model compared to the Langmuir isotherm, as it is an empirical equation that accounts for the heterogeneity of sites and the exponential distribution of sites and their energy. This model does not make assumptions about the maximum amount of substance that can be adsorbed per unit area or about the constancy of the substance's ability to be adsorbed.[48] The linear version of the Freundlich isotherm was used for the adsorption of MNZ,[49] as represented by the equation:

$$\log q_e = \log K_F + \frac{1}{n} \log C_e \tag{7}$$

where the variable q_e represents the quantity of MNZ adsorbed in mg g^{-1}, C_e is the equilibrium concentration of the MNZ (mg L^{-1}), and K_F and n are Freundlich constants that influence the adsorption capacity. The Freundlich isotherm, which was utilized to analyze the adsorption of MNZ on the surface of PCN-600-NS-10, was determined to be unsuitable due to its negative slope.

The Dubinin–Radushkevich isotherm model was also employed to assess the equilibrium adsorption data of MNZ. This model is commonly utilized to describe the adsorption mechanism onto heterogeneous surfaces, characterized by a Gaussian energy distribution. It is particularly suitable for representing adsorption equilibrium within a moderate range of adsorbate concentration.[50] The adsorption isotherm under consideration exhibited similarities to the Langmuir isotherm. The methodology above distinguishes between physical and

chemical adsorption based on the mean free energy. The linear expression of the Dubinin–Radushkevich model is stated below.[51]

$$\ln q_e = \ln q_m - \beta e^2 \tag{8}$$

$$e = RT \ln\left(1 + \frac{1}{C_e}\right) \tag{9}$$

$$E = \frac{1}{\sqrt{2\beta}} \tag{10}$$

where the symbol β represents a constant that is associated with the mean free energy of adsorption; the variable q_e denotes the quantity of MNZ adsorbed in mg g^{-1}; the variable q_m represents the maximum amount of MNZ that may be adsorbed in a monolayer, also measured in mg g^{-1}; the variable e corresponds to the Polanyi potential; R denotes the universal gas constant; T represents the absolute temperature; and E signifies the mean adsorption energy. The present study established that the Dubinin–Radushkevich isotherm yielded the most favourable results for the adsorption phenomenon of MNZ, as evidenced by the high values of the regression co-efficient ($R^2 = 0.999$). Furthermore, the range of mean free energy, as estimated by this model (100–129.1 J mol^{-1}) and as presented in Table 3, suggests that the adsorption process was of a physisorption character. According to the Dubinin–Radushkevich model, the adsorption phenomenon is primarily associated with the filling of micropore volumes rather than occurring through a layer-by-layer adsorption mechanism on the surfaces of the material.[11]

2.13. Degradation mechanism of MNZ

The by-products of MNZ degradation were analyzed using liquid-chromatography mass-spectrometry (LC-MS), as shown in Fig. S8 of the ESI Section.† The suggested process for breaking down MNZ involves a series of reactions, including hydroxylation, bond-scission, and ring-cleavage. The reactions take place in the presence of hydroxyl radicals (OH˙) and superoxide radicals (O₂˙⁻). The probable breakdown of MNZ *via* two possible routes is suggested based on the identified intermediates shown in Fig. 6. Fig. 6 shows that the MNZ molecule ($m/z = 171$) underwent a process where hydroxide and carbonyl species were increased, leading to the creation of 2-(4-hydroxy-5-nitro-1*H*-imidazole-1-yl) acetic acid ($m/z = 187$). Substituting the hydroxide with a nitro-group produces an intermediate with an m/z of 140.3 (2-(4,5-dihydroxy-1*H*-
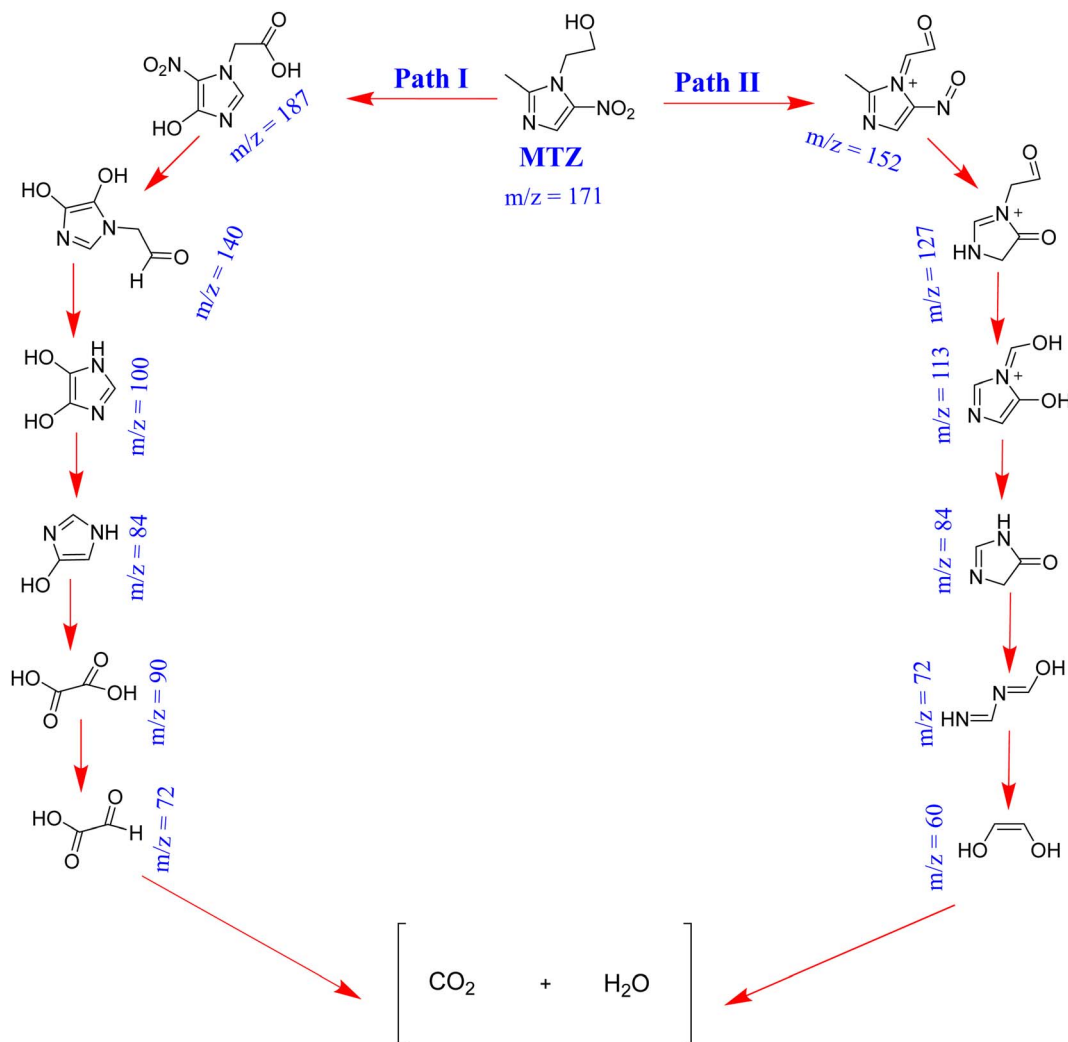
Fig. 6 Proposed degradation pathway of metronidazole.

imidazole-1-yl) acetaldehyde). This molecule undergoes a transition to 1H-imidazole-4,5-diol ($m/z = 100.31$) through the removal of an aldehydic group. The hydroxylation reaction generates intermediates, like 1H-imidazole-4-ol with an m/z of 84.2. The ring-opening reaction subsequently generates intermediates, including oxalic acid ($m/z = 90.38$) and 2-oxo-acetic acid ($m/z = 72.7$).

In pathway II, the MTZ molecule undergoes degradation through the oxidation of $^•OH/O_2^{•-}$ to produce its initial intermediate ((1Z)-2-methyl-5-nitroso-1-(2-oxoethylidene)-1H-imidazole-1-ium), which had an m/z of 152.1. The second fragment, which had an m/z of 127.3 (4-oxo-3-(2-oxoethyl)-4,5-dihydro-1H-imidazile-ium), was produced when the OH$^•$ radical attacked and removed the NO$_2$ group. It was subsequently degraded into two unstable intermediates with m/z values of 113.19 (5-hydroxy-1-hydroxymethylene-1H-imidazole-1-ium) and 84.18 (3,5-dihydroxy-4H-imidazole-4-one). The fragment with an m/z of 72.7 (N-(iminomethyl)formidic acid) was generated through the ring opening of 3,5-dihydroxy-4H-imidazole-4-one via the attack of the $O_2^{•-}$ radical. Conversely, the ethene

diol fragment, which had an m/z of 60.3, was obtained through an OH$^•$ radical attack.

2.14. Identification of reactive oxygen species (ROS)

Experiments involving the trapping of free radicals were conducted to identify the primary active species responsible for the photocatalytic degradation of MNZ (metronidazole). In this study, three scavengers—isopropanol (IPA), triethanolamine (TEOA), and p-benzoquinone (p-BQ)—were employed to selectively quench specific reactive oxygen species (ROS): hydroxyl radicals (OH$^{•-}$), positive holes (h$^+$), and superoxide radicals ($O_2^{•-}$), respectively. The results indicated that the removal efficiency of PCN-600-NS-10 decreased from 87% to 76% upon the addition of p-BQ, suggesting that superoxide radicals ($O_2^{•-}$) played a relatively minor role in the photocatalytic degradation of MNZ using the PCN-600-NS-10 photocatalyst.

On the other hand, introducing TEOA and IPA into the photocatalytic system resulted in more significant decreases in removal efficiency. Specifically, the removal efficiency dropped from 87% to 63% with TEOA and to 43% with IPA. This implies

that hydroxyl radicals (OH$^{\bullet}$) and positive holes (h^{+}) had a substantial influence as the principal reactive oxygen species (ROS) in the degradation mechanism of MNZ using the PCN-600-NS-10 photocatalyst. To gain further insights into the generation of reactive radicals, electron paramagnetic resonance (EPR) spectroscopy was employed. Spin-trapping agents, namely 5,5-dimethylpyroline-oxide (DMPO) and 2,2,6,6-tetramethyl-4-piperidine (TEMPO), were utilized to identify the radicals produced within the experimental system. The results presented in Fig. 7 from the EPR analysis demonstrate the detection of signals corresponding to hydroxyl radicals (OH$^{\bullet}$) and positive holes (h^{+}) following irradiation. The signal intensities of these species showed a significant increase over time, providing substantial evidence for the formation of ROS during the photocatalytic process. In contrast, the signals corresponding to superoxide radicals (O$_2^{\bullet-}$) were significantly low, indicating their limited involvement in the degradation process of MNZ. We can conclude that the combination of radical trapping experiments and EPR analysis supports the conclusion that hydroxyl radicals (OH$^{\bullet}$) and positive holes (h^{+}) played a predominant and synergistic role in controlling the photocatalytic degradation process of MNZ when using the PCN-600-NS-10 photocatalyst. These findings contribute valuable insights into the mechanistic aspects of the photocatalytic degradation of MNZ and the specific ROS involved in this process.

Table 4 Adsorption and photocatalytic degradation of MNZ using recycled PCN-600-NS-10; conditions: dose = 0.02 g L^{-1}, concentration of MNZ = 20 mg L^{-1}, pH = 6, room temperature

Reusable number	Weight	Removal (%)		Total removal (%)
		Adsorption	Degradation	
1st	0.02	44	50	94
2nd	0.018	39	46	85
3rd	0.017	37	49	84
4th	0.017	36	48	84
5th	0.016	35	48	82

3. Experimental

The materials are detailed in S1 of the ESI.†

3.1. Synthesis of PCN-600

PCN-600 was synthesized by the reported method in ref. 19 with some modifications. Briefly, Fe(NO$_3$)$_3\cdot$9H$_2$O (80 mg), TCPP (80 mg), and trifluoroacetic acid (2.4 mL) were ultrasonically dissolved in 16 mL of DMF in a 20 mL Pyrex vial. The mixture was then heated at 150 °C in an oven for 12 h. The resulting samples were cooled down to ambient temperature, washed with DMF three times, and finally dried at 70 °C overnight.
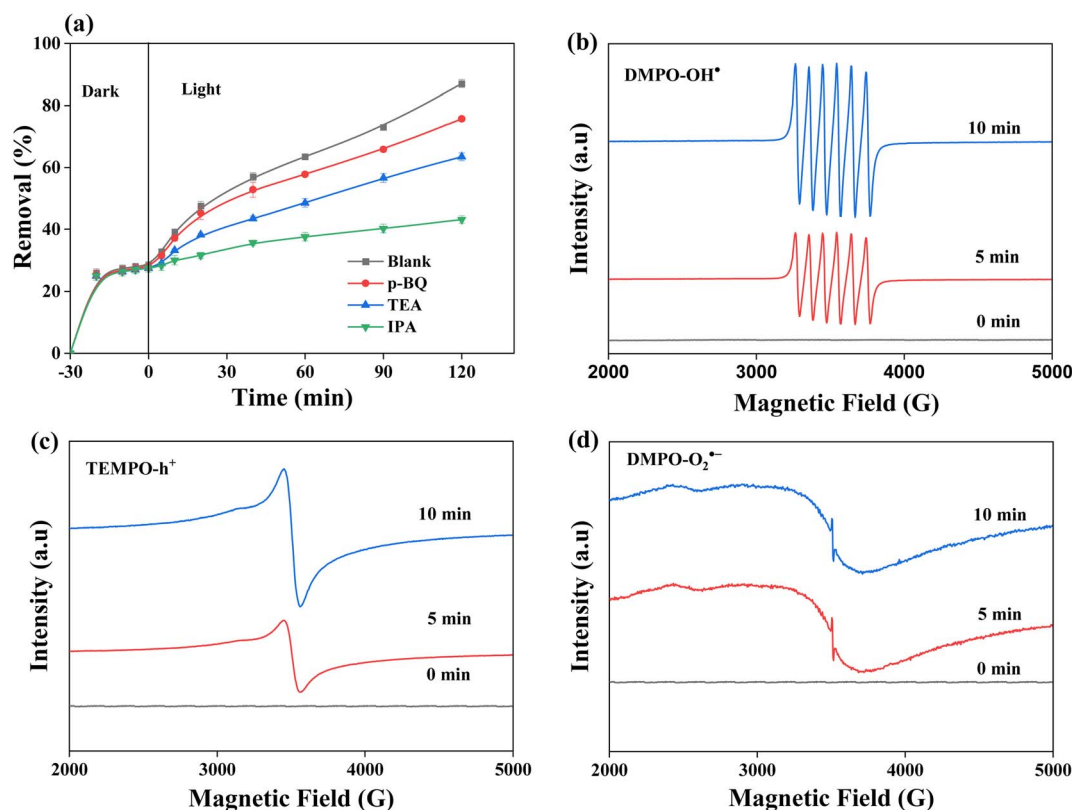

Fig. 7 (a) Effect of radicals' scavengers on the degradation performance of MNZ using PCN-600-NS-10. EPR spectra in different system: (b) DMPO-% OH$^{\bullet}$-adducts, (c) TEMP-h^{+} adducts, (d) DMPO-O$_2^{\bullet-}$ %-adducts (experimental conditions: catalysts = 10 mg L^{-1}, initial pH = 6, [DMPO] = 20 mM, [TEMP] = 20 mM).

3.2. Doping of the NS-ligand into PCN-600

The *in situ* synthesis approach was employed for co-doping of the NS-ligand into PCN-600. In the synthesis process, Fe(NO$_3$)$_3$·9H$_2$O (80 mg), TCPP (80 mg), 1,2-benzisothiazole-3-one (10 mg), and trifluoroacetic acid (2.4 mL) taken in 16 mL of DMF were ultrasonically dissolved in a 20 mL Pyrex vial. The mixture was heated in a 150 °C oven for 12 h. The resulting samples were cooled down to room temperature, washed with DMF twice, and dried at 80 °C overnight. The final product obtained was named PCN-600-NS-10. The same procedure obtained another sample except that the amount of NS-ligand treated was 20 mg and it was named as PCN-600-NS-20.

3.3. Adsorption and photocatalytic degradation

The compound metronidazole (MNZ) was dissolved in deionized water to obtain a stock solution with a concentration of 100 mg L^{-1}. The experimental solutions of MNZ were obtained from the stock solution by dilution. In this study, PCN-600 and PCN-600 doped with varying concentrations of NS-ligand were employed for the adsorption-assisted photocatalytic degradation of MNZ. The adsorption and photocatalytic degradation tests were conducted using a 250 mL glass beaker, in which 100 mL of the reaction mixture was placed. The pH of the solution was subsequently modified to the intended value using a 0.1 M solution of HCl or NaOH. Before irradiation, a specific quantity of each sample was introduced into a solution of MNZ at a particular concentration. The resulting mixture was agitated for 30 min in a dark environment to ensure that adsorption–desorption equilibrium was achieved. The adsorption capabilities of PCN-600, PCN-600-NS-10, and PCN-600-NS-20 were evaluated in a solution of MNZ under dark conditions at ambient temperature.

The degradation experiments used a visible-light lamp with a power output of 200 W. The lamp was positioned 1 foot above the sample. This setup irradiated the solution. The reactor was magnetically stirred to achieve a uniform dispersion of the solution. Samples were collected at specific time intervals following adsorption and irradiation. These samples were then subjected to centrifugation at a speed of 4000 revolutions per min for 10 min to eliminate any suspended particles present in the solutions. Subsequently, the samples were analyzed with a UV-visible spectrophotometer. The experiments were conducted in triplicate, and the standard deviation did not surpass 5%. The calculations of the MNZ removal effectiveness, expressed as the percentage of adsorption and degradation, as well as the adsorption capacity q_m in units of mg g^{-1}, at various time intervals, were performed using the following equations:

$$\text{Removal (\%)} = (C_0 - C_t)\frac{V}{m} \quad (11)$$

$$\text{Adsorption capacity}(q_m) = (C_0 - C_e)\frac{100}{C_0} \quad (12)$$

where C_0, C_t, and C_e represent the initial concentration, concentration at time t, and equilibrium concentration of the MNZ, respectively; V denotes the volume of the solution in litres; and m represents the mass of the adsorbent in grams.

Details of the characterizations are provided in S2 of the ESI.†

3.4. Regeneration and reusability

Evaluating the feasibility of PCN-600-NS-10 for cost-effective and environmentally friendly water treatment methods hinges on its regeneration and reusability. To evaluate this, the photocatalyst underwent five successive cycles, and its capacity for reuse was examined. The detailed procedure was as follows: the reused sample, at a concentration of approximately 0.02 g L^{-1}, was immersed successively in a tube in 5 mL of water, acetone, and ethanol. This mixture underwent ultrasonication for 10 min and subsequent centrifugation, with the process repeated three times for each solvent. After washing, the regenerated sample was dried overnight at 80 °C to activate it in the next cycle. Table 4 illustrates that the total removal efficiency of the PCN-600-NS-10 catalyst declined from 94% to 82% over five consecutive cycles. The percentage of MNZ removal *via* adsorption consistently decreased after regeneration, indicating an incomplete desorption by the catalyst. Notably, the 3rd, 4th, and 5th cycles demonstrated a higher contribution of degradation to elimination compared to the 2nd cycle. The reduced adsorption capacity after the first cycle led to a higher concentration of MNZ available for degradation in subsequent cycles. Moreover, the catalyst showed incomplete regeneration, as evidenced by a decrease in weight after the initial cycle (Table 4), resulting in a reduced total removal efficiency. The outcomes of the regeneration and reuse experiments underscore that PCN-600-NS-10, synthesized through the *in situ* approach, is a cost-effective material with consistent adsorptive and photocatalytic capabilities across multiple cycles.

Furthermore, a comparison of the removal of metronidazole between our catalyst (PCN-600-NS-10) and some others reported in the literature was made and is summarized in Table S1 of the ESI Section.† As compared to the other reported photocatalysts, PCN-600-NS-10 synthesized in our study exhibited a higher adsorption capacity and higher removal rate with a lower dose.

4. Conclusions

This study presents the development of a strategy for incorporating an NS-ligand into PCN-600 by a one-pot *in situ* process. The potential synergistic effects resulting from the incorporation of the NS-ligand into the PCN-600 metal–organic framework (MOF) were investigated and evaluated for efficacy for the removal of MNZ from aqueous solutions. The experimental results demonstrated that the PCN-600 MOF, doped with the N–S-ligand, exhibited enhanced adsorption and catalytic capabilities compared to the unmodified MOF for the removal of MNZ from wastewater when subjected to visible-light irradiation. The mechanisms of adsorption and degradation were studied using models based on pseudo-second-order and pseudo-first-order kinetics, respectively. The negative values for standard ΔG_{ads} and ΔG_{ads} indicated that the adsorption of MNZ was

a spontaneous, viable, and exothermic process. The positive value of ΔS_{ads} indicated the increased randomization at the solid–liquid interface during MNZ adsorption. The identification of reactive oxygen species through the utilization of trapping and electron paramagnetic resonance (EPR) investigations revealed that hydroxyl radicals (OH$^\bullet$) and photogenerated holes (h$^+$) were the primary active species involved in the process of the photocatalytic degradation of MNZ. The experimental findings indicated that the PCN-600-NS-10 sample exhibited excellent stability and reusability throughout five cycles. This study presents a potentially effective method for the treatment of wastewater containing antibiotics, such as metronidazole.

Conflicts of interest

The authors declare no competing financial interest.

Acknowledgements

Notes and references

1 A. Ahmed, M. Usman, Z. Ji, M. Rafiq, R. Ullah, B. Yu, Y. Shen and H. Cong, *J. Environ. Chem. Eng.*, 2023, **11**, 110452.

2 S. A. Mirsalari, A. Nezamzadeh-Ejhieh and A. R. Massah, *Environ. Sci. Pollut. Res. Int.*, 2022, **29**, 33013–33032.

3 D. Wang, F. Jia, H. Wang, F. Chen, Y. Fang, W. Dong, G. Zeng, X. Li, Q. Yang and X. Yuan, *J. Colloid Interface Sci.*, 2018, **519**, 273–284.

4 Y. L. Wang, A. Gómez-Avilés, S. Zhang, J. J. Rodriguez, J. Bedia and C. Belver, *J. Environ. Chem. Eng.*, 2023, **11**, 109744.

5 E. Shahnazari-Shahrezaie and A. Nezamzadeh-Ejhieh, *RSC Adv.*, 2017, **7**, 14247–14253.

6 H. Derikvandi and A. Nezamzadeh-Ejhieh, *J. Hazard. Mater.*, 2017, **321**, 629–638.

7 M. Rafiq, A. Ahmed, M. Usman, R. Ullah, F. Gao, M. Mateen, B. Yu, Y. Shen and H. Cong, *J. Environ. Chem. Eng.*, 2023, 111608, DOI: 10.1016/j.jece.2023.111608.

8 R. Fahrig and M. Engelke, *Mutat. Res., Genet. Toxicol. Environ. Mutagen.*, 1997, **395**, 215–221.

9 S. Kim and D. S. Aga, *J. Toxicol. Environ. Health, Part B*, 2007, **10**, 559–573.

10 A. Yousefi, A. Nezamzadeh-Ejhieh and M. Mirmohammadi, *Environ. Technol. Innovation*, 2021, **22**, 101496.

11 R. Ullah, J. Sun, A. Gul and S. Bai, *J. Environ. Chem. Eng.*, 2020, **8**, 103852.

12 X. Tang, Q. Feng, K. Liu and T. Yan, *Mater. Lett.*, 2016, **183**, 175–178.

13 X. Li, K. Peng, H. Chen and Z. Wang, *Sci. Rep.*, 2018, **8**, 11663.

14 R. Ullah, C. Liu, H. Panezai, A. Gul, J. Sun and X. Wu, *Arabian J. Chem.*, 2020, **13**, 4092–4101.

15 H. Dong, G. Zeng, L. Tang, C. Fan, C. Zhang, X. He and Y. He, *Water Res.*, 2015, **79**, 128–146.

16 S. Hu, M. Liu, F. Ding, C. Song, G. Zhang and X. Guo, *J. CO2 Util.*, 2016, **15**, 89–95.

17 A. Khan, K. Talha, W. Bin, J.-H. Liu, R. Ullah, F. Feng, J. Yu, S. Chen and J.-R. Li, *J. Environ. Chem. Eng.*, 2019, **8**, 103642.

18 J. Gordon, H. Kazemian and S. Rohani, *Mater. Sci. Eng., C*, 2015, **47**, 172–179.

19 X.-X. Huang, L.-G. Qiu, W. Zhang, Y.-P. Yuan, X. Jiang, A.-J. Xie, Y.-H. Shen and J.-F. Zhu, *CrystEngComm*, 2012, **14**, 1613–1617.

20 F. Guo, R.-X. Li, S. Yang, X.-Y. Zhang, H. Yu, J. J. Urban and W.-Y. Sun, *Angew. Chem., Int. Ed.*, 2023, **62**, e202216232.

21 Z. Shams-Ghahfarokhi and A. Nezamzadeh-Ejhieh, *Mater. Sci. Semicond. Process.*, 2015, **39**, 265–275.

22 A. Dhakshinamoorthy, Z. Li and H. Garcia, *Chem. Soc. Rev.*, 2018, **47**, 8134–8172.

23 W. Li, S. Wu, H. Zhang, X. Zhang, J. Zhuang, C. Hu, Y. Liu, B. Lei, L. Ma and X. Wang, *Adv. Funct. Mater.*, 2018, **28**, 1804004.

24 X. Hou, J. Wang, B. Mousavi, N. Klomkliang and S. Chaemchuen, *Dalton Trans.*, 2022, **51**, 8133–8159.

25 Y. Bai, Y. Dou, L.-H. Xie, W. Rutledge, J.-R. Li and H.-C. Zhou, *Chem. Soc. Rev.*, 2016, **45**, 2327–2367.

26 A. Dhakshinamoorthy, A. M. Asiri and H. Garcia, *Adv. Mater.*, 2019, **31**, 1900617.

27 S. Navalón, A. Dhakshinamoorthy, M. Álvaro, B. Ferrer and H. García, *Chem. Rev.*, 2023, **123**, 445–490.

28 A. Dhakshinamoorthy, A. M. Asiri and H. García, *Angew. Chem., Int. Ed.*, 2016, **55**, 5414–5445.

29 L. Sun, J. Xie, Z. Chen, J. Wu and L. Li, *Dalton Trans.*, 2018, **47**, 9989–9993.

30 G. C. Shearer, S. Chavan, S. Bordiga, S. Svelle, U. Olsbye and K. P. Lillerud, *Chem. Mater.*, 2016, **28**, 3749–3761.

31 S. A. Mirsalari and A. Nezamzadeh-Ejhieh, *Sep. Purif. Technol.*, 2020, **250**, 117235.

32 N. Mehrabanpour, A. Nezamzadeh-Ejhieh, S. Ghattavi and A. Ershadi, *Appl. Surf. Sci.*, 2023, **614**, 156252.

33 Alamgir, K. Talha, B. Wang, J.-H. Liu, R. Ullah, F. Feng, J. Yu, S. Chen and J.-R. Li, *J. Environ. Chem. Eng.*, 2020, **8**, 103642.

34 M. Aram, M. Farhadian, A. R. Solaimany Nazar, S. Tangestaninejad, P. Eskandari and B.-H. Jeon, *J. Mol. Liq.*, 2020, **304**, 112764.

35 A. N. Ejhieh and M. Khorsandi, *J. Hazard. Mater.*, 2010, **176**, 629–637.

36 A. Rahmani-Aliabadi and A. Nezamzadeh-Ejhieh, *J. Photochem. Photobiol., A*, 2018, **357**, 1–10.

37 N. Nasseh, B. Barikbin, L. Taghavi and M. A. Nasseri, *Composites, Part B*, 2019, **159**, 146–156.

38 Alamgir, K. Talha, Y.-J. Wang, R. Ullah, B. Wang, L. Wang, W. Wu, S. Chen, L.-H. Xie and J.-R. Li, *RSC Adv.*, 2021, **11**, 23838–23845.

39 F. Yu, S. Sun, S. Han, J. Zheng and J. Ma, *Chem. Eng. J.*, 2016, **285**, 588–595.

40 T. Kalhorizadeh, B. Dahrazma, R. Zarghami, S. Mirzababaei, A. M. Kirillov and R. Abazari, *New J. Chem.*, 2022, **46**, 9440–9450.

41 Y. Tang, X. Zhang, X. Li, J. Bai, C. Yang, Y. Zhang, Z. Xu, X. Jin and Y. Jiang, *Sep. Purif. Technol.*, 2023, **322**, 124305.

42 P. Mohammadyari and A. Nezamzadeh-Ejhieh, *RSC Adv.*, 2015, **5**, 75300–75310.

43 Y. S. Ho and G. McKay, *Process Biochem.*, 1999, **34**, 451–465.

44 N. Liu, H. Wang, C.-H. Weng and C.-C. Hwang, *Arabian J. Chem.*, 2018, **11**, 1281–1291.

45 Z. A. Piskulich, O. O. Mesele and W. H. Thompson, *J. Phys. Chem. A*, 2019, **123**, 7185–7194.

46 T. Chen, T. Da and Y. Ma, *J. Mol. Liq.*, 2021, **322**, 114980.

47 J. Wang and X. Guo, *Chemosphere*, 2020, **258**, 127279.

48 A. Nezamzadeh-Ejhieh and M. Kabiri-Samani, *J. Hazard. Mater.*, 2013, **260**, 339–349.

49 H.-K. Chung, W.-H. Kim, J. Park, J. Cho, T.-Y. Jeong and P.-K. Park, *J. Ind. Eng. Chem.*, 2015, **28**, 241–246.

50 N. Ayawei, A. N. Ebelegi and D. Wankasi, *J. Chem.*, 2017, **2017**, 3039817.

51 Q. Hu and Z. Zhang, *J. Mol. Liq.*, 2019, **277**, 646–648.